Particle dynamics and current-free double layers in an expanding, collisionless, two-electron-population plasma

G. Hairapetian[a] and R. L. Stenzel
Department of Physics, University of California, Los Angeles, California 90024-1547

(Received 20 August 1990; accepted 15 November 1990)

The expansion of a two-electron-population, collisionless plasma into vacuum is investigated experimentally. Detailed *in situ* measurements of plasma density, plasma potential, electric field, and particle distribution functions are performed. At the source, the electron population consists of a high-density, cold ($kT_e \simeq 4$ eV) Maxwellian, and a sparse, energetic ($\frac{1}{2}mv_e^2 \simeq 80$ eV) tail. During the expansion of plasma, space-charge effects self-consistently produce an ambipolar electric field whose amplitude is controlled by the energy of tail electrons. The ambipolar electric field accelerates a small number ($\sim 1\%$) of ions to streaming energies which exceed and scale linearly with the energy of tail electrons. As the expansion proceeds, the energetic tail electrons electrostatically trap the colder Maxwellian electrons and prevent them from reaching the expansion front. A potential double layer develops at the position of the cold electron front. Upstream of the double layer both electron populations exist; but downstream, only the tail electrons do. Hence, the expansion front is dominated by retarded tail electrons. Initially, the double layer propagates away from the source with a speed approximately equal to the ion sound speed in the cold electron population. The propagation speed is independent of the tail electron energy. At later times, the propagating double layer slows down and eventually stagnates. The final position and amplitude of the double layer are controlled by the relative densities of the two electron populations in the source. The steady-state double layer persists till the end of the discharge ($\Delta t \simeq 1$ msec), much longer than the ion transit time through the device ($t \simeq 150\,\mu$sec). On the low-potential side, the double layer generates a monoenergetic, neutralized ion beam with no stationary background plasma. The field-aligned double layer contains no trapped or counter-streaming ions, and is current free; i.e., the relative electron–ion drift is zero.

I. INTRODUCTION

It is well known that when a high-density plasma expands into vacuum or a low density background plasma, ions are accelerated to supersonic velocities[1-4] during the expansion. The process of ion acceleration has been observed in laboratories since the 1930s when investigators[5,6] working with vacuum arc experiments had detected high velocity plasma jets in low-pressure *dc* discharges. In 1961, Plyutto[7] for the first time proposed the process of plasma expansion as a possible mechanism for acceleration of ions. Plyutto postulated that in an expanding plasma the lighter, more mobile electrons would tend to escape into vacuum faster than the heavier ions, and thereby generate a self-consistent ambipolar electric field that would accelerate the ions and retard electrons. In 1966, Gurevich, Pariiskaya, and Pitaevskii[1] analytically solved the one-dimensional, time-dependent problem of plasma expansion, and obtained a set of approximate solutions, called self-similar solutions, which predicted the acceleration of ions to very high energies. Since these early works, the phenomenon of plasma expansion has been linked to a number of seemingly diverse physical situations which occur in a wide spectrum of plasmas ranging from the high-density, high-temperature laser-fusion[8,9] plasmas to the low-density, low-temperature space[10,11] plasmas.

As early as 1969, it was suggested[11] that plasma expansion is directly related to the problem of the interaction of terrestrial plasma with rapidly moving bodies such as satellites and planets. When a body travels supersonically through a plasma, a density cavity[12] is created on its wake side which the surrounding plasma attempts to fill. A natural mechanism for the filling of the wake[12,13] is the free expansion of the ambient plasma into the cavity. In laser-fusion experiments,[14,15] the laser light heats and ionizes a solid pellet, and generates a high-density, high-temperature plasma. The high-density plasma along with the vaporized target material expand radially outward, and the recoil momentum compresses the target to achieve thermonuclear fusion.[16,17] To improve the efficiency of target implosion, a basic understanding of the plasma expansion process and subsequent ion acceleration is vital.[18] Singh and Schunk[19] have suggested that the basic physical process occurring in the polar wind[20] can be described in terms of plasma expansion. According to the model, the high-density ionospheric plasma expands along the earth's magnetic field lines into the magnetosphere, and in the process ionospheric ions (H^+ and O^+) are accelerated into the magnetosphere. In addition, the process of plasma expansion has also been speculated to be active in solar wind outflow from coronal holes,[21] formation of ion beams in plasma sheet boundary layer,[22] active chemical release experiments in space,[23] refilling of depleted flux tubes after a magnetic storm,[24] and interaction of supernova with the interstellar medium.[25] In light of the fact that plasma expansion has a great deal of possible applications in a number of active research fields, the expansion process has been investigated in several laboratory experiments. A large

[a] Present address: Department of Electrical Engineering, University of California, Los Angeles, California 90024-1547.

 0899-8221/91/040899-16$02.00

number of experiments[13,26-30] have been conducted to specifically study the process of filling of the wakes. An obstacle is usually placed in a streaming plasma to model satellites moving through space plasma. The streaming plasma flows supersonically past the obstacle and creates a void or "vacuum" immediately behind the obstacle. Biased and floating obstacles of various shapes and compositions have been used to study the filling of the void by the surrounding plasma. At least two major mechanisms[31] have been identified for filling of wakes. The first mechanism is the free expansion of plasma, and the second is the deflection of ions into the wake by the obstacle's sheath electric field.[32] The obstacle bias with respect to the surrounding plasma potential determines which mechanism dominates.

A second group of laboratory experiments have been performed to exclusively study the expansion of the plasma into vacuum. Various experimental configurations such as Q machines,[33] triple-plasma devices,[34] and pulsed plasma sources[35] have been used to investigate the expansion phenomenon. Initially a high-density plasma is either created locally or confined by grids; subsequently, the plasma is allowed to expand into a vacuum chamber. In general, these laboratory experiments have confirmed some of the predicted self-similar behavior including ion acceleration, and density rarefaction. Ion velocities as high as ten times the sound speed have been reported.[35]

A third group of experiments have studied the process of expansion in laser produced plasmas.[3,15,18,36,37] Because of the high temperature and high density of the laser-produced plasmas, details of the plasma expansion and ion acceleration are difficult to observe. For example, the anomalously high-velocity ions emitted from the target are detected by a Faraday cup[38] or a Thomson mass spectrometer[18] placed outside of the vacuum chamber, at large distances away from the target. The dynamics of the plasma expansion and ion acceleration which in some cases occur in nanosecond time scales and over spatial regions of a few millimeters are only inferred from the external measurements.

Except for laser-pellet experiments, the experimental investigation of the plasma expansion has been limited to single-electron-temperature, Maxwellian plasmas. The more complicated and interesting case of the non-Maxwellian plasma expansion has not been fully investigated experimentally. In laser-pellet experiments, x-ray[39] and $K\alpha$ line[40] emission measurements have shown that the electron distribution function is a non-Maxwellian with an energetic tail. It is speculated[9,41,42] that the fast tail electrons are responsible for generation of low-density, anomalously high-velocity ions which carry away up to half of the absorbed laser energy and reduce the efficiency of target implosion. Evidence for non-Maxwellian plasma expansion also exists in some active space experiments. For example, in the Star-of-Lima experiment, where the process of critical ionization of a dense neutral cloud of barium is studied, satellite measurements[43] have shown three distinct electron populations with different temperatures in the barium plasma. It is postulated[44] that the energetic electrons could have a significant effect on ionization and expansion of the plasma cloud.

In this paper, we describe in detail a laboratory experiment where a plasma with a non-Maxwellian electron distribution consisting of a Maxwellian and an energetic tail is allowed to expand into a large, high vacuum chamber. Evolution of plasma potential profile and particle distribution function are measured *in situ* over a very long expansion length; and a detailed picture of ion dynamics and electric field evolution is obtained during the expansion. Since the expanding plasma contains energetic electrons, the background neutral density must remain low during the expansion to eliminate ionizing or charge-exchange collisions with the background gas. As will be demonstrated later, the presence of even a low-pressure ($P \geqslant 2\times10^{-5}$ Torr) background neutral gas drastically modifies the expansion of the plasma. A new plasma source is developed which locally creates a relatively dense, pulsed discharge plasma while maintaining a low background pressure ($P \leqslant 2\times10^{-6}$ Torr). The highly reproducible, pulsed plasma source allows detailed *in situ* measurements of the temporal and spatial evolution of the plasma during its expansion into vacuum. To our knowledge, no measurements of ion distribution and electric field profiles in an expanding non-Maxwellian plasma have been performed, with the exception of two Letters[45,46] on this work.

II. EXPERIMENTAL ARRANGEMENT

The experiment is performed in a large cylindrical (80 cm diam, 170 cm length), high-vacuum ($P_{\text{base}} \simeq 3\times10^{-7}$ Torr) chamber (Fig. 1). A set of external coils produces a uniform ($\Delta B/B \leqslant 5\%$), magnetic field ($B_0 \simeq 0$–50 G). The discharge ($V_{\text{dis}} \simeq 30$–120 V, $I_{\text{dis}} \simeq 1$–20 A) is produced locally by a filamentary cathode consisting of a set of 18 tungsten filaments, 14 cm long and spaced 0.5 cm apart. The filaments are heated by a dc power supply which is switched off during discharge ($\Delta t \simeq 1$ msec) so as to create monoenergetic primary electrons with an isotropic shell distribution. A grid anode is located behind the cathode (separation $\simeq 0.5$ cm); and at the backside of the source, a floating electrode is mounted to reduce the wall effects. The cathode is normally connected to chamber wall (ground). The source-plasma is created at the anode potential ($V \simeq +30$–120 V) by ionizing a collimated neutral (ar-

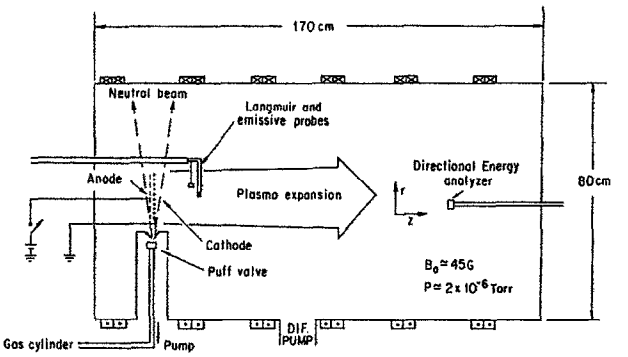

FIG. 1. Schematic side view of the experimental device (not to scale). The radially injected neutral beam is locally ionized by energetic source electrons. The plasma expands axially along an externally applied magnetic field.

gon) beam. The pulsed ($t_{on} \simeq 1$ msec, $t_{off} \simeq 3$ sec) neutral beam is injected radially into the source, and is ionized quickly ($t \simeq 5$–$10\,\mu$sec) by the discharge electrons. Through continuous pumping, the background neutral pressure is maintained below $P \simeq 2 \times 10^{-6}$ Torr during the discharge.

The pulsed neutral beam is produced in a small cylindrical (15 cm diam, 35 cm length) chamber with a separate pumping stage. The two chambers are connected to each other by a collimating orifice through which the neutral gas is injected into the main chamber. A modified, piezoelectric leak valve[47] regulates the gas flow. The normally closed leak valve is activated by applying a high voltage pulse ($V \simeq 300$ V) to the piezoelectric crystal. The valve opens rapidly (full closed to full open in $t < 100\,\mu$sec) against a high back pressure (40–60 psi) allowing the high density gas to expand supersonically through the nozzle orifice (2 mm diam). Because of rapid expansion, the gas molecules are accelerated to supersonic velocities while their random thermal energy decreases.[48] Initially, the gas flow is highly collisional (laminar flow). However, as it expands, the gas density decreases and the flow becomes molecular. The supersonic, collisionless gas jet is then collimated by a sharp-edged skimmer before injection into the main chamber. Because of the low duty cycle of the valve ($t_{rep} \simeq 3$ sec) and two-stage pumping, a very low background pressure ($P < 2 \times 10^{-6}$ Torr) is maintained in the main chamber. The axial density profile of the radially injected neutral gas is measured in the main chamber with a small (2.5 cm long, and 1 cm diam), moveable ionization-gauge probe[49] which consists of a miniature pentode (6AH6) with the glass tube removed. The probe has a linear response in the pressure range of 10^{-6}–10^{-3} Torr, and its response time is better than 75 μsec. Figure 2 shows the temporal evolution of the axial pressure profile. The measurements are performed along the central axis ($r = 0$) of the circular plasma source (diam $\simeq 10$ cm), and at a radial distance of about 7.5 cm from the nozzle orifice. As can be seen in Fig. 2, the bulk of the neutral density is concentrated at $z = 0$ (plasma source), and the axial expansion of the neutral along the z axis is insignificant even at $t \simeq 1$ msec. Without the skimmer, the axial density profile of the neutral beam is broader by a factor of 3.

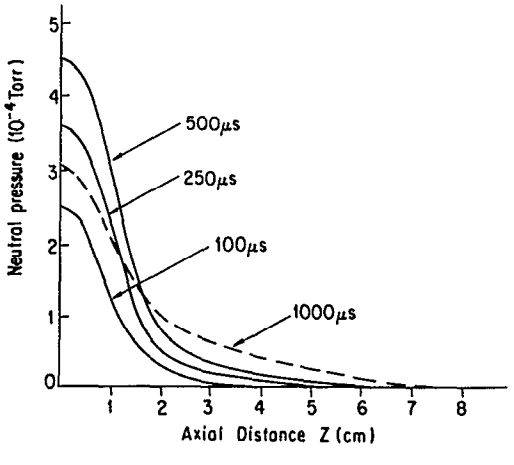

FIG. 2. The temporal evolution of the axial neutral pressure profile at $r = 0$. The neural gas is injected radially at $r = -5$ cm; the circular plasma source extends from $r = -5$ cm to $r = +5$ cm. The piezoelectric valve is activated at $t = -650\,\mu$sec, and the discharge pulse is turned on at $t = 0\,\mu$sec.

The neutral beam is ionized by the energetic electrons emitted by the cathode and collected by the anode. The strong axial density gradient of the neutral beam limits ionizing and charge exchange collisions to the vicinity of the source. In the rest of the chamber, the very low background pressure makes atomic collisions, both elastic and inelastic, negligible. The calculated ion-neutral collision mean-free path[50] for charge-exchange collisions is 30 m. The electron–neutral collisions mean-free paths[50] are 40 m for elastic collisions, and over 400 m for ionizing collisions. This feature of the experiment is very unique and is not found in other discharge plasmas where the background neutral pressure is one to two orders of magnitude higher ($5 \times 10^{-4} \geqslant P \geqslant 5 \times 10^{-5}$ Torr). The pulsed discharge plasma expands supersonically along an axial magnetic field and reaches the end of the chamber in $t \simeq 100\,\mu$sec. The axial magnetic field confines the electrons radially ($r_e \simeq 0.5$ cm) and produces a plasma column of 12 cm diam which is roughly equal to the cathode diameter. The ions are unmagnetized. The source plasma consists of Maxwellian electrons ($kT_e \simeq 4$ eV), cold Maxwellian ions ($kT_i < 0.5$ eV), and a small number of energetic primary electrons which are emitted by the cathode. The source plasma is neutral; i.e., $n_i = n_M + n_{tail}$ where n_i, n_M, and n_{tail} are the ion density, the Maxwellian electron density, and the energetic tail electron density, respectively. Typically, the ratio n_{tail}/n_M is less than 5% at the source. The basic parameters of the plasma outside the source are summarized in Table I.

The source plasma expands rapidly into vacuum because of its strong pressure gradient. As the plasma expands, the faster discharge electrons stream into vacuum first while the less energetic Maxwellian electrons and the heavier ions lag behind. The space-charge separation self-consistently generates an electric field which retards the electrons and accelerates the ions. The expansion proceeds at the ion velocity. During the expansion, the two electron populations separate with the energetic tail electrons dominating the expansion front. The expanding plasma is probed by a variety of movable emissive probes, directional energy analyzers, various size Langmuir probes, and microwave resonator probes. A brief description of each diagnostic unit follows.

Plasma potential is measured with an emissive probe mounted on a movable, L-shaped probe shaft. The emissive probe (0.1 mm diam, 3 mm long tungsten wire) is heated by a dc power supply. During the measurement, the heater leads are disconnected mechanically by a relay, and the floating potential of the probe is measured by a fast buffer. To reduce cable capacitance, the relay and the buffer are mounted on the probe shaft, inside the chamber, and at a close distance ($\ell \simeq 17$ cm) to the tip of the emissive probe. The emissive probe is shielded, and has a capacitance of 15 pF to ground. Figure 3(a) shows schematically the emissive probe and the buffer circuit. The I-V characteristics of the probe are traced out to confirm that the floating potential of

TABLE I. Basic plasma parameters.

Neutral gas, pressure ($z \geqslant 10$ cm)	Argon, $P \simeq 2\times 10^{-6}$ Torr
Density	$n_e \simeq 10^9 - 10^{11}$ cm^{-3}
Electron temperature	$kT_e \simeq 4$ eV
Ion temperature	$kT_i \leqslant 0.5$ eV
Tail electrons	
energy	$\frac{1}{2}mv_e^2 \simeq 80$ eV
relative density	$n_{tail}/n_e \leqslant 5\%$ at the source ($z \simeq 0$)
Electron plasma frequency	$f_{pe} \simeq 0.28$–2.8 GHz
Ion plasma frequency	$f_{pi} \simeq 1$–10 MHz
Debye length	$\lambda_D \simeq 0.05$–0.9 mm
Magnetic field	$B_0 \simeq 10$–50 G
Electron cyclotron frequency	$f_{ce} \simeq 28$–140 MHz
Ion cyclotron frequency	$f_{ci} \simeq 0.38$–1.9 KHz
Electron cyclotron radius	$r_{ce} \simeq 0.1$–1.3 cm
Ion cyclotron radius	$r_{ci} \simeq 13$–65 cm
Elastic electron–neutral collisions (Ref. 50)	
frequency	$\nu_{en} \simeq 1\times 10^5$ sec^{-1}
mean-free path	$\ell_{en} \simeq 4\times 10^{-3}$ cm
Charge-exchange (Ar^+ in Ar) collisions (Ref. 50)	
frequency	$\nu_{in} \simeq 2.5\times 10^2$ sec^{-1}
mean-free path	$\ell_{in} \simeq 3\times 10^{-3}$ cm
Ionizing Collisions (Ref. 50)	
frequency	$\nu_{ion} \simeq 1.1\times 10^3$ sec^{-1}
mean-free path	$\ell_{ion} \simeq 4.9\times 10^{-4}$ cm
Electron–electron collision frequency (Ref. 51)	$\nu_{ee} \simeq 1.0\times 10^3 - 6.2\times 10^5$ sec^{-1}
Electron–ion collision frequency (Ref. 51)	$\nu_{ei} \simeq 3.0\times 10^2 - 2.5\times 10^5$ sec^{-1}

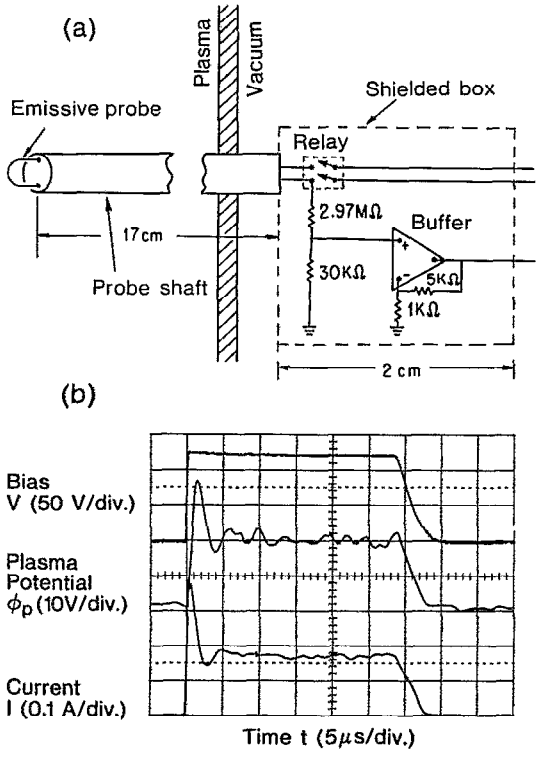

FIG. 3. (a) Schematic view of the emissive probe along with the buffer circuit for measuring the floating potential. (b) Probe response to a large positive potential (+ 120 V) applied to an electrode. Displayed is also the electron current collected by the electrode.

the emissive probe matches well with the plasma potential. The probe response time is measured by applying a fast, positive pulse ($V \simeq 120$ V, 100 nsec rise time, 30 μsec wide) to a large electrode (3 cm diam) immersed in the plasma, and recording the time response of the emissive probe. The floating potential of the emissive probe rises (36 V in $t < 1$ μsec, falls (16 V in $t \simeq 2$ μsec), and then remains approximately constant (+ 20 V over the prepulse value of the plasma potential) till the end of the pulse [Fig. 3(b)]. A large positive sheath develops around the electrode to shield out the applied positive potential. The emissive probe floating potential and the electron current collected by the electrode have very similar waveforms; i.e., an initial overshoot[52] followed by a constant value.

The electron and ion distribution functions are measured with a directional retarding-grid energy analyzer[32] (2 cm in diam and 1 cm wide). The directional analyzer has an energy resolution of 0.5 eV, and can measure the angular divergence of a monoenergetic beam to within its angular resolution ($\Delta\theta \simeq 6°$). The absolute value of the electron density is measured with a microwave resonator probe.[53] The probe consists of small resonator, a $\lambda/4$ parallel-wire transmission-line section with one end shortened and one end open. The resonance is excited and observed via a transmission line. A resonator of length ℓ immersed in a uniform medium of dielectric constant ϵ, exhibits resonance at

$$\omega_{res} = (\pi/2\ell)(c/\sqrt{\epsilon}). \quad (1)$$

In a field-free plasma where $\epsilon = 1 - (\omega_p^2/\omega^2)$, the reso-

nance frequency is increased from the value in vacuum $[\omega_{0res} = (\pi c/2\ell)]$ to

$$\omega_{res}^2 = \omega_{0res}^2 + \omega_p^2. \quad (2)$$

By measuring the resonance frequencies in vacuum and in plasma, one can easily deduce the plasma frequency $(\omega_p^2 = n_e e^2/\epsilon_0 m)$ or electron density. The above analysis also holds in magnetized plasmas as long as $\omega_p^2 \gg \omega_c^2$. The spatial resolution of the probe is determined by its size which is typically between 5.0 ($f_{res} \simeq 1.5$ GHz) to 6.5 cm ($f_{res} \simeq 1.15$ GHz) long and about 1 cm wide. Where possible, the density measurements are also performed by Langmuir probes which compare well (to within 20 %) to those obtained by the resonator probe. Various size Langmuir probes are also used to measure the radial plasma density profile, the electron temperature, and the relative densities of the Maxwellian to the energetic tail electrons.

III. MEASUREMENT RESULTS

The experimental observations are divided into two parts. The first part deals with the initial stage of plasma expansion into vacuum,[45] and the second part deals with the subsequent evolution[46] of the plasma after expansion into vacuum is completed.

A. Initial expansion of plasma

In the initial stages of the expansion, the highly localized discharge plasma expands rapidly into the highly evacuated vacuum chamber ($p \leqslant 2\times10^{-6}$ Torr). Time-of-flight measurements indicate that the plasma front propagates and reaches the end of the chamber (length $\simeq$ 130 cm) in about 100 μsec (average velocity $\simeq 1.3\times10^6$ cm/sec). Since no background plasma exists, the faster electrons must be neutralized by the slower source ions (thermal velocity $v_{th} \simeq 1\times10^5$ cm/sec) which during the expansion process are accelerated to an average velocity of $v_{avg} \simeq 1.3\times10^6$ cm/sec. The directional energy analyzer is used to resolve the energy and distribution function of ions.

1. Ion distribution

The ion distribution function is measured with the directional energy analyzer which is mounted on a movable, axial shaft. The analyzer is facing the source, and its surface normal is parallel to the external magnetic field. The collector electrode of the analyzer is biased to $V_c = -130$ V (to collect ions and reject electrons) while the microchannel plate is allowed to float (to reflect most electrons and pass ions). At each axial position, the discriminator bias is changed in increments of 0.5 V, and the ion flux is averaged over ten shots, recorded, and stored for each discriminator bias setting. The analyzer is moved axially along the central axis of plasma in increments of 10 cm and the process is repeated. Subsequently, the current-voltage characteristics of the analyzer are reconstructed at each spatial position as a function of time, smoothed and differentiated once to obtain the parallel ion distribution function. Figure 4 shows the normalized ion distribution functions versus energy at $t = 100\,\mu$sec for several axial positions. Near the source,

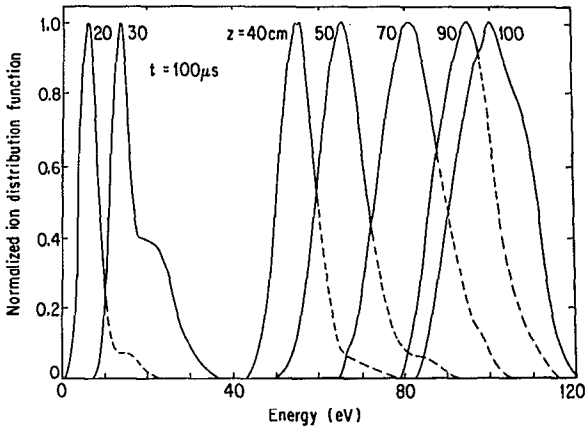

FIG. 4. Normalized, parallel ion distribution function obtained from the derivatives of the directional analyzer characteristics. The beamlike distributions are measured on the central axis of the plasma at $t = 100\,\mu$sec. The beam streaming energy increases as a function of axial distance from the source.

only the thermal ions ($kT_i < 1$ eV) are observed. As the distance from the source increases, the kinetic energy of ions (measured at the peak of the distribution function) increases and energetic tails begin to form. A sudden increase in the ion kinetic energy is observed at $z \simeq 35$ cm. Thereafter, the ions are further accelerated at a decreasing rate. The accelerated ions have a beamlike distribution with their streaming energy far exceeding their temperature.

The cold source ions are accelerated, and form an energetic ion beam whose streaming energy increases as a function of axial distance from the source. The angular divergence of the ion beam is measured by rotating the directional analyzer (angular resolution $\Delta\theta \simeq 6°$) about a radial axis. Figure 5 shows the normalized ion beam current as a function of angle θ between the collector normal and the incident beam direction at $z \simeq 60$ cm for two different times. The ion beam has a narrow angular divergence with a half-width of $\Delta\theta \simeq 7°$ at $t \simeq 50\,\mu$sec, which broadens to $\Delta\theta \simeq 9°$ at $t \simeq 100\,\mu$sec. The angular broadening is due to a decrease in

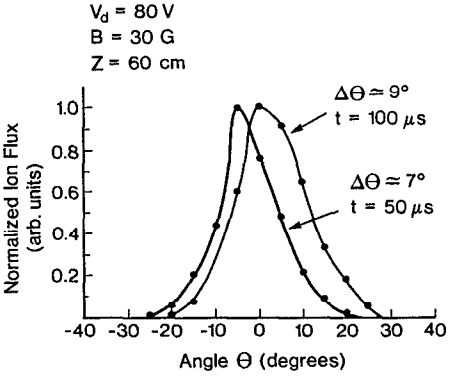

FIG. 5. Normalized ion beam current as a function of angle θ between the beam direction and the analyzer normal. The angular spread $\Delta\theta$ (half-width at half-maximum) is a quantitative measure of $v_\perp/v_\parallel$. The narrow angular profiles indicate that, to a good approximation, ions are accelerated one-dimensionally along the magnetic field lines. As a function of time, the angular profile broadens because of a decrease in the parallel velocity of ions.

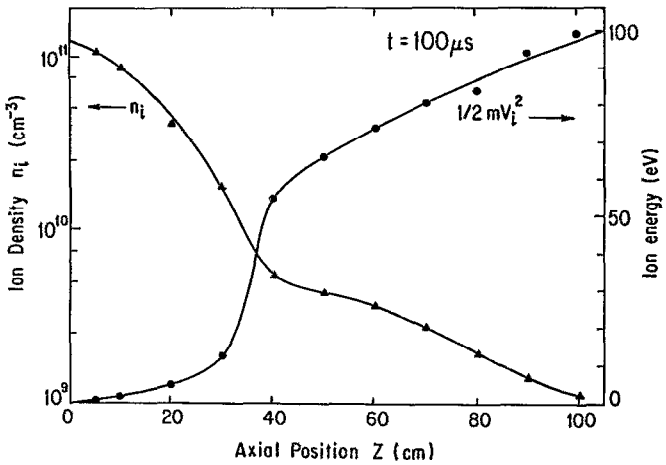

FIG. 6. Ion density and streaming energy profiles at $t = 100\,\mu$sec. Ion density decreases away from the source while its kinetic energy increases. A very small number of ions ($\sim 1\%$) are accelerated to energies exceeding that of the electrons (80 eV).

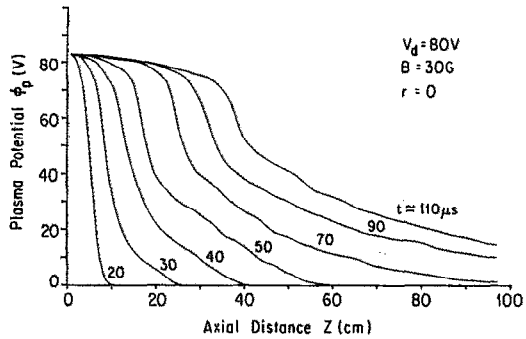

FIG. 7. Measured temporal evolution of the axial plasma potential profile. As a function of time, a steplike structure similar to a double layer develops. The ions gain most of their energy while traversing the double layer.

the parallel streaming velocity of the beam as a function of time. The observed angular spread is a quantitative measure of relative parallel and perpendicular velocities of the ions ($\tan\theta = v_\perp/v_\parallel$). For a purely one-dimensional acceleration, the perpendicular velocity of ions is due to its initial thermal spread. In our case, the ion thermal spread at the source is $kT_i \leqslant 0.5$ eV, and the expected angular spread at $t = 50\,\mu$sec and $t = 100\,\mu$sec are 4.1° and 4.8°, respectively. Therefore, to within the angular resolution ($\Delta\theta \simeq 6°$) of the analyzer, the ion acceleration is approximately one dimensional.

The energy analyzer is calibrated to also measure the density of ions. The kinetic energy and density of ions at $t \simeq 100\,\mu$sec are both displayed versus the axial distance in Fig. 6. As a function of distance, the ion density n_i decreases while its streaming energy increases. There exists a continuous spectrum of ion energies with the high-density ($n_i \simeq 10^{11}$ cm^{-3}) thermal ions at the source and the sparse ($n_i \leqslant 10^9$ cm^{-3}) highly energetic ions at the expansion front. At $z = 100$ cm, ions reach a streaming energy of 100 eV well in excess of the tail electron energy (80 eV). The maximum measured ion streaming energy is $\frac{1}{2}Mv_i^2 \simeq 120$ eV. During the expansion, the input discharge power is partially converted into energetic ions. It is instructive to estimate the power conversion efficiency. The average total ion power is given by $P_{\text{ion}} = n_i(\frac{1}{2}Mv_i^2)v_iA$ where n_i, v_i, and M are the ion density, velocity, and mass, respectively; and A is the plasma cross section. The energetic ions have approximately an average density of 10^9 cm^{-3} and a maximum energy of 120 eV; and the plasma cross-sectional area is 150 cm^2. Then, the average ion power is $P_i \simeq 7$ W which is less than 1% of the discharge power (800 W). Hence, only a small fraction ($< 1\%$) of the input discharge power is converted into fast ions while the rest is primarily lost at the anode.

2. Plasma potential and electric field

The axial, ambipolar electric field responsible for ion acceleration is deduced from the plasma potential measurements. The measurements are performed by the emissive probe on the central axis of plasma over a distance of 100 cm and in increments of $\Delta z \simeq 1$ cm. At each axial position, the floating potential of the emissive is averaged over 10 shots, recorded and stored for processing in a computer. Subsequently, the plasma potential profiles are reconstructed for different times. Figure 7 shows the time evolution of the axial plasma potential profile. At the source, the plasma potential approximately assumes the anode potential ($+80$ V). The plasma expansion is initiated by the primary (tail) electrons ($\frac{1}{2}mv_e^2 \simeq 80$ eV) which expand into vacuum first due to their high velocity. The space-charge separation induces a potential gradient ($\Delta\phi \simeq 80$ V, $\Delta z \simeq 4$ cm) which reflects the electrons and accelerates ions. As a function of time the potential gradient broadens axially and propagates away from the source (Fig. 8). At later times ($t > 40\,\mu$sec), a localized steplike structure known as a double layer begins to emerge in the potential profile. Ions gain a large fraction of their streaming energy while traversing the double layer.

The potential profiles are differentiated once to yield the electric field ($E_z = -\Delta\phi_p/\Delta z$). As noted earlier, the electric field propagates away from the source, its profile broadens axially, and its amplitude decreases (Fig. 8). At the position of the double layer, the electric field profile displays a well-defined peak. The cold Maxwellian electrons

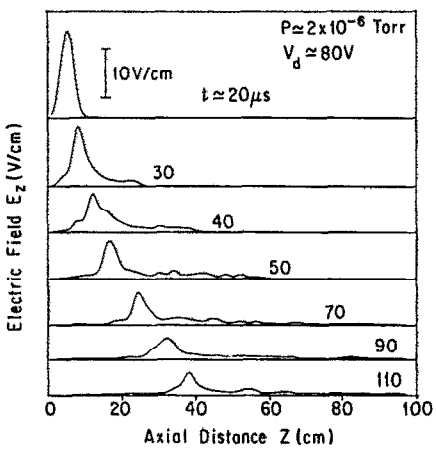

FIG. 8. Axial electric field profiles obtained from derivatives $-d\phi/dz$ of the electrostatic potential.

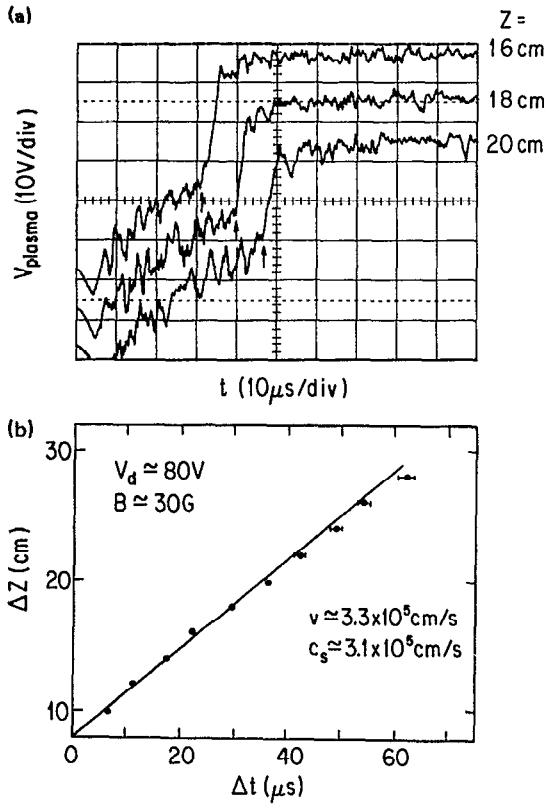

FIG. 9. Propagation of the double layer. (a) Temporal profiles of the plasma potential as measured with the emissive probe for different probe positions. (b) Plot of the axial probe position versus the temporal position of the double layer.

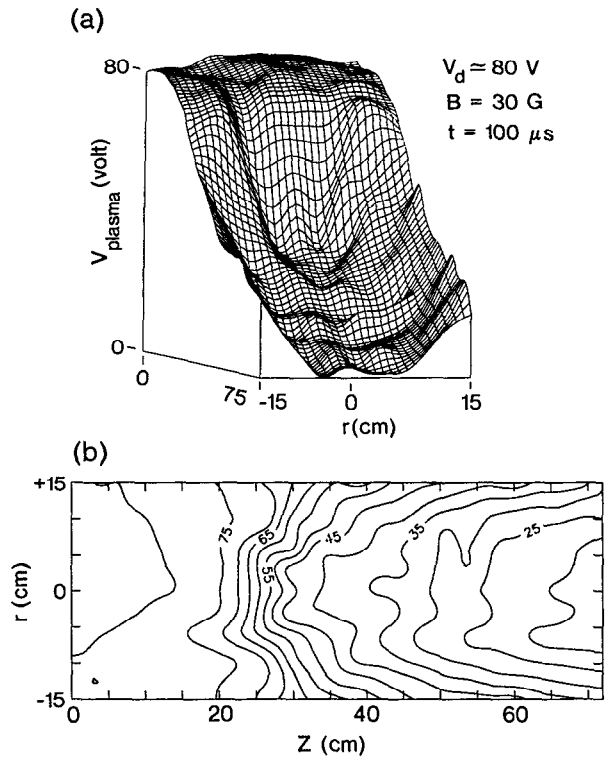

FIG. 10. (a) Two-dimensional plasma potential profile as a function of z and r at $t = 100\,\mu$sec. (b) The corresponding contours of constant plasma potential ($\Delta\phi = 5$ V between contours).

($kT_e \simeq 4$ eV) are electrostatically confined by the double layer ($\Delta\phi \simeq 30$ eV). Therefore, downstream of the double layer the electron population consists only of the retarded energetic tail electrons. Physically, the double layer marks the position of the Maxwellian electron front ahead of which their density is negligible. The double layer propagates away from the source (Fig. 9) at $v \simeq 3.3 \times 10^5$ cm/sec which happens to correspond approximately to the ion acoustic speed ($C_s \simeq 3.1 \times 10^5$ cm/sec) in the cold ($kT_e \simeq 4$ eV) Maxwellian plasma. It is worthwhile to mention that ions stream faster than the double layer. The propagation velocity of the double layer is independent of the energy of the energetic electrons, but does depend on the initial density gradient of the source plasma and the density ratio of the two electron species (n_{tail}/n_M). As will be shown later, the double-layer velocity ranges from 1.5×10^5 to 3.7×10^5 cm/sec which is of the order of the ion sound speed corresponding to the cold electrons. At the double layer, strict charge neutrality is violated. The excess space-charge density within the double layer can be inferred from the axial gradient of the electric field profiles ($n_i - n_e = \epsilon_0 dE_z/e\,dz$). Normalized to the local plasma density, the maximum excess charge density is less than 0.1% which is beyond resolution of any probe.

It has been shown[42,54] theoretically that the presence of a small number of energetic tail electrons enhances ion acceleration. Furthermore, for the case of a two-electron-temperature expanding plasma, numerical solutions[41,55,56] and particle simulations[57,58] results show the formation of a hydrodynamic shock (i.e., a potential double layer). Since the potential drop $\Delta\phi$ across the double layer (shock) is estimated to be of the order of the hot electron temperature (kT_h/e), the colder electrons ($kT_c \leqslant kT_h/10$) are predicted to be electrostatically trapped by the double layer. Across the double layer, the electron distribution function changes abruptly with the retarded tail electrons dominating the low-potential region.

The plasma potential is also mapped in two dimensions. Because of the cylindrical geometry, the potential is measured only in axial and radial directions. Figure 10 displays the plasma potential as a function of r and z at $t = 100\,\mu$sec, along with the contours of constant potential. Since the electrons are magnetized, they are confined magnetically to within a cylindrical tube whose diameter is equal to that of the cathode (diameter $\simeq 10$ cm). Within the tube, the potential gradient is mainly axial, while outside, it is radial. As expected, most of the axial potential gradient is concentrated within the double layer. The shape of the potential contours indicates that ions in the center of the plasma column are accelerated mainly in the z direction, which agrees with the ion distribution measurements. The radially inward directed electric fields which electrostatically confine the unmagnetized ions develop due to magnetic confinement of the electrons. As the magnetic field is reduced, the radially inward electric field begins to change direction (Fig. 11), and becomes radially outward for the case of very low external magnetic field. At very low axial magnetic fields, the lighter, more mobile electrons diffuse radially to the grounded chamber wall faster than the heavier ions, and as a result a

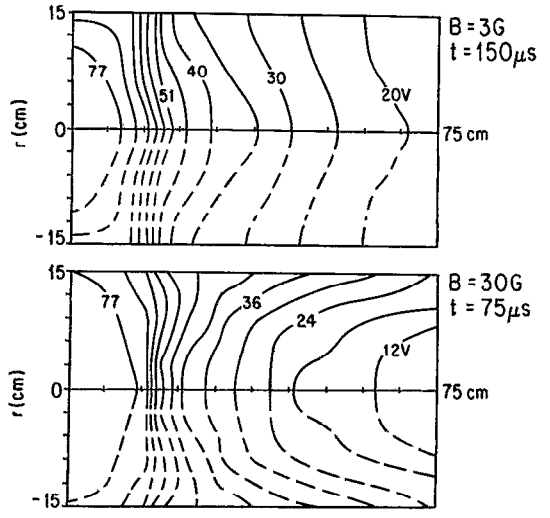

FIG. 11. Plasma potential contours for two different values of axial magnetic field strength. The profiles show a radially inward directed electric field which becomes radially outward at low magnetic fields. The solid lines represent the measured data while the dashed lines are the mirror images.

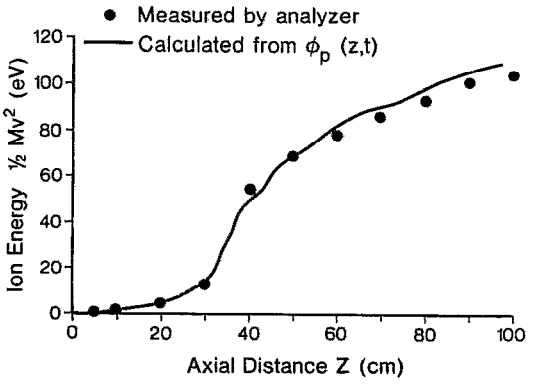

FIG. 12. The calculated energy gain from the moving ambipolar electric field for a test Ar^+ ion. The test ions are injected continuously into the field at $z = 0$ with an initial energy of 0.1 eV. At $t = 100\,\mu$sec, the computed total kinetic energy of each test particle is displayed against its axial position (solid line). For comparison purposes, the measured ion kinetic energies are also displayed.

radially outward ambipolar electric field develops to retard the radial diffusion of electrons.

The presence of energetic ($\frac{1}{2}mv_e^2 = \epsilon_e$) electrons limits the potential drop $\Delta\phi$ at the plasma vacuum interface to ϵ_e/e. This is in contrast to the case of a purely Maxwellian plasma where the potential drop is unlimited; i.e., $\Delta\phi = (kT_e/e)\ln(n/n_0)$. Despite a finite potential drop, some ions gain more energy than indicated by the stationary electrostatic potential drop; i.e., $\frac{1}{2}Mv^2 > e\Delta\phi$. A careful examination of the temporal evolution of the electric field profile reveals a qualitative explanation. As a function of time, the electric field profile propagates, broadens, and occupies a larger region, even though $\Delta\phi$ (area under the curve) remains constant. Ions whose transit time through the electric field exceed the time rate of change of the electrostatic field, spend a longer time in the field, and are accelerated for a longer time (distance), and as a result gain more energy than in a stationary electric field. In principle, given a potential profile $\phi(z,t)$, one can calculate the kinetic energy that a test particle can acquire from the field. Since the electrostatic potential is measured in great detail in space and time, a computer code is written to calculate in one dimension (z direction) the energy gained by the particle and to quantitatively demonstrate the ion transit time effects. It must be stressed that the purpose of the calculation is to gain a further understanding of the motion of a single particle in a moving electric field, and is not a computer simulation of the experiment. In the computation, each test particle (Ar^+) has an initial parallel velocity of $v_i \simeq 5\times 10^4$ cm/sec which corresponds to a thermal energy of $kT_i \simeq 0.1$ eV. The particles are injected individually into the electrostatic field in time increments of 0.1 μsec. Each particle is advanced in z by $\Delta z = v(z,t)\Delta t (\Delta t = 10$ nsec), and the change in its velocity is computed from

$$\Delta v(z,t) = \{2(e/M)[\phi(z,t) - \phi(z+\Delta z,t)]\}^{1/2}, \quad (3)$$

where the values of $\phi(z,t)$ are interpolated from the measured potential profile. Subsequently, z and t are advanced by Δz and Δt, respectively, and the values of $v(z,t)$ and $E_z(z,t)$ are updated. Next, the particle is further advanced by Δz and the iterative process is repeated. The computation is halted after $t = 100\,\mu$sec, and the kinetic energy of each particle is recorded as a function of its axial position. The test particles injected in earlier times fully traverse the axial electric field profile and gain the highest energy while the particles injected at later times are accelerated for a much shorter time and acquire the lowest energy. Figure 12 displays both the measured and calculated values of the energy gain as a function of axial distance at $t = 100\,\mu$sec. A surprisingly good agreement (to within 10%) exists between the calculated and observed values considering the fact that the measured ion energies represent a time-averaged streaming energy of an ion beam. As can be seen, some of the ions are accelerated to energies which exceed the electrostatic potential drop ($\frac{1}{2}Mv_i^2 > e\Delta\phi$).

As mentioned above, the excess energy gained by the ions is due to ion transit time effects. To better understand this effect, the ion transit time is varied in the above calculations by varying the mass of the test ions. For each case, the ion energy gain is calculated and plotted against its mass (Fig. 13). The lighter ions traverse the potential well before the potential profile changes (propagates) appreciably, and as a result gain roughly the full potential energy ($e\Delta\phi \simeq 83$ eV) of the electrostatic electric field. As the ion mass increases, the time that each ion spends in the propagating potential well increases, and its gain in energy exceeds the potential energy. Finally, the very massive ions lag behind the faster moving potential well and end up gaining only a fraction of the potential energy.

The dependence of the maximum kinetic energy of ions on the energy of the tail electrons is investigated by varying the tail electron energy. The energy of tail electrons which is determined by the discharge voltage is varied in increments of 10 eV from 50 to 120 eV. For each case, the ion distribution functions are obtained from the current-versus-discriminator voltage characteristics of the analyzer located at $z \simeq 110$ cm. As before, the ions have a beamlike distribution.

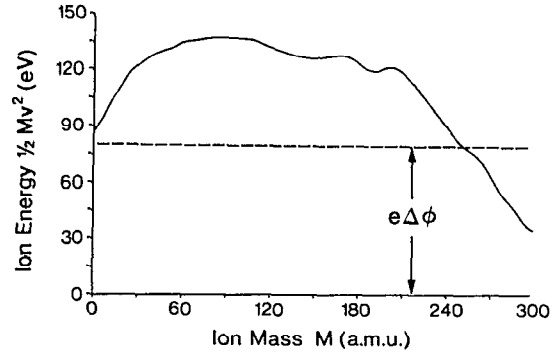

FIG. 13. Calculated ion energy gain as a function of ion mass. The ion transit time through the electric field is controlled by the ion mass. The lighter, more mobile ions gain approximately the full electrostatic potential drop $\Delta\phi$(83 eV), while the very massive, slower ions lag behind the moving electric field and gain only a fraction of $\Delta\phi$.

The beam streaming energy has no sharp maxima, and decreases continuously as a function of time while the beam density increases. The highest measured ion beam energy is limited by the signal-to-noise ratio. Figure 14 shows the maximum beam energy (measured at the peak of the distribution function) plotted against the corresponding tail electron energy. The measurements show that the maximum ion beam energy exceeds the tail electron energy by 30–40 eV, and scales linearly with the electron energy.

3. Electron temperature and density

The electron temperature and density is measured with a Langmuir probe which consists of a small tantalum disk (diameter = 0.3 cm). Near the source, the electron temperature ($kT_e \simeq 4$ eV) and density ($n_e \simeq 10^{11}$ cm^{-3}) are readily determined from the probe current-versus-voltage characteristics. Probe measurements indicate that the electron population consists of a high-density Maxwellian (n_M), and a small percentage of energetic tail electrons ($n_{tail}/n_M \leqslant 0.05$). The tail electrons have a shell distribution. During the expansion, the Maxwellian electrons are confined by the large ambipolar electric field set up by the tail electrons. The Maxwellian electrons form a well-defined front which is marked by the double layer.[40,55,57] Upstream of the double layer, the electron population consists of the Maxwellian and tail electrons; but downstream, only the tail electrons exist. On the downstream side where the tail electrons dominate, the probe characteristics display no electron saturation region; i.e., the electron density cannot be measured. Therefore, the relative density profile of the plasma in the radial direction is measured with the Langmuir probe biased to collect ion saturation current. The radial profiles are bell shaped with a half-width at half-maximum of about $\Delta r \simeq 6$ cm, and show very little radial broadening as a function of axial distance from the source. This indicates that the radial expansion of plasma is negligible as asserted earlier.

The absolute electron density is measured with the microwave resonator probe which is mounted on an axially movable probe shaft. The resonator (5–6.5 cm long) is oriented radially to improve its axial resolution. Since the plasma density changes as a function of time, the applied microwave frequency ω is kept constant while the time varying plasma sweeps through ω. Figure 15 shows the ion saturation current [15(a)] and the resonator output signal as a function of time [15(b)]. The resonator signal displays a resonance peak at a particular time (density). The sharpness of the peak is determined by the time rate of change of the density. As the applied microwave frequency is increased the resonance occurs at later times (higher plasma densities). At each axial position, the temporal electron density profile is measured; and the process is repeated at several different axial positions to obtain the temporal evolution of the axial electron density profile. Because of the small space-charge separation [$(n_e - n_i/n_e) \leqslant 0.1\%$], the electron and ion densities are practically identical. Figure 16 displays the temporal evolution of the axial density and the corresponding plasma potential profiles along the central axis. The measured density is actually an average density over the radial length of the resonator. The results indicate that as the plasma expands, the high-density source plasma rarefies and its

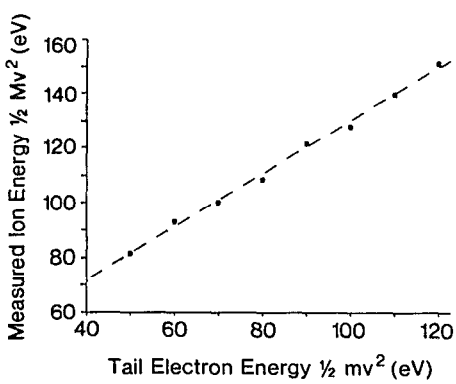

FIG. 14. The dependence of the maximum ion kinetic energy on the tail electron energy. The ion energy is measured with the directional energy analyzer located at $z \simeq 110$ cm, $r \simeq 0$.

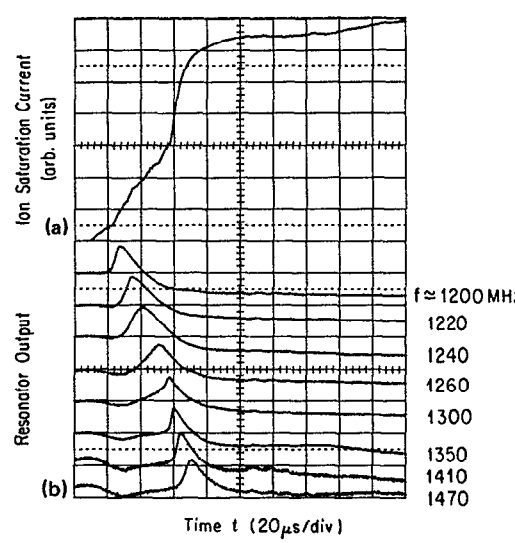

FIG. 15. (a) Ion saturation current as a function of time. (b) The microwave resonator output signal for different values of applied microwave frequency. As the frequency is increased the resonance occurs at later times (higher densities).

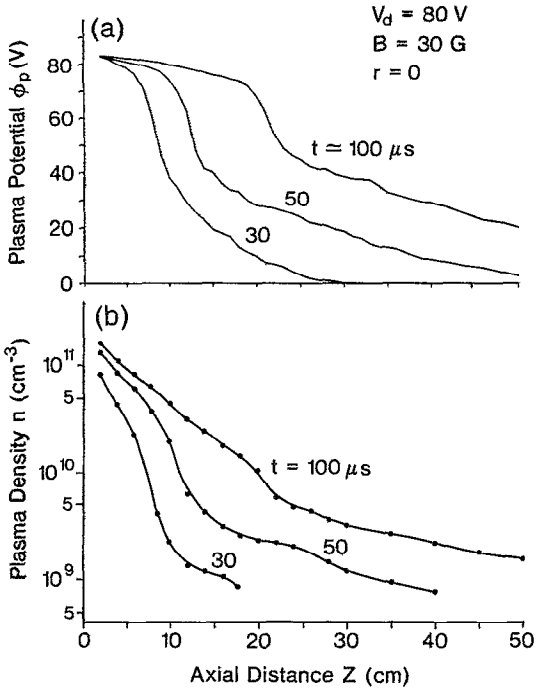

FIG. 16. (a) Plasma potential profiles are shown for different times. (b) The corresponding plasma density is measured with the microwave resonator probe.

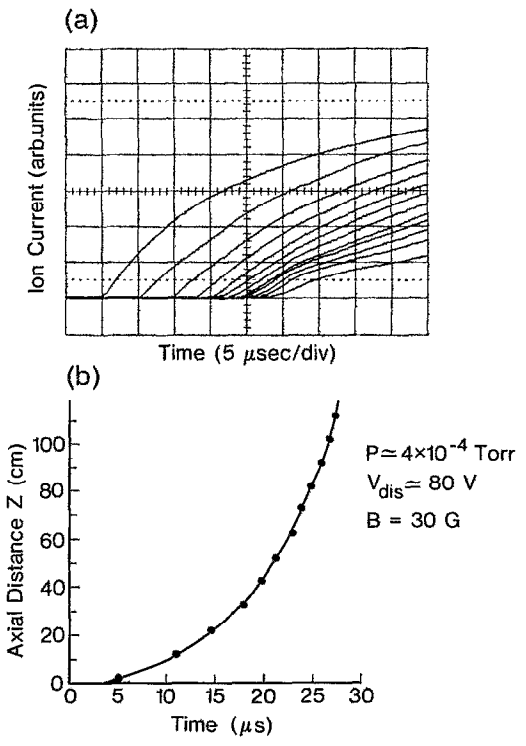

FIG. 17. Propagation of plasma front at high background pressures $P \simeq 4\times 10^{-4}$ Torr. (a) Measured ion current as a function of time for different axial positions of detector. (b) Time-of-flight diagram of the plasma front.

density drops by almost two and a half order of magnitude. The density gradient displays a sharp break (a knee) at the position of the double layer.

4. Effects of background gas

To study the effects of the background gas on the expansion process, the experiment is performed at several different background neutral pressures. For $P = 4\times 10^{-4}$ Torr, Fig. 17(a) shows the ion saturation current as a function of time for increasing detector distance from the source. As opposed to the case of low neutral pressure, the ion current waveform shows a well-defined ion front. The detector is moved away from the source at increments of 10 cm and the ion flux is recorded at each position. The velocity of plasma front is obtained by plotting the detector position versus the arrival time of ion front [Fig. 17(b)]. The time-of-flight measurements indicate that the plasma front accelerates away from the source with velocities approaching $v \simeq 7\times 10^6$ cm/sec which translates into a kinetic energy of about 1 keV for ions. The plasma front velocity decreases with decreasing neutral pressure. At pressures below 2×10^{-5} Torr, the well-defined plasma front disappears, and an accurate time-of-flight measurement cannot be performed.

The above observations would indicate that ions are accelerated to extremely high energies even at very high background neutral pressures. The directional analyzer was used to independently measure the energy of ions. In contrast to the time-of-flight measurements, the analyzer shows that most ions at the plasma front are cold and stationary. The two apparently conflicting results can be explained in terms of ionization of the background neutrals. At high background pressures, the energetic electrons ionize the background gas and create an electron–ion pair. The newly created electrons stream back toward the positive source while the ions neutralize the excess electron charge at the plasma front and enable the energetic electrons to propagate into the neutral gas. As the neutral density is increased, the ionization frequency (ω_{ion}) increases; the excess space charge is neutralized faster ($\sim 1/\omega_{ion}$); and the electrons can propagate at a higher speed through the background gas. At very low neutral pressures ($p \leqslant 2\times 10^{-6}$ Torr), the charge neutralizing ions are created in the source region only. Therefore, charge neutralization occurs over an ion transit time. Since the excess negative space charge must be neutralized before the electrons can propagate, the propagation velocity is limited by the velocity of ions. It must be pointed out that even at higher background pressures the ionization front velocity ($v \sim 10^7$ cm/sec) is much lower than the expected velocity of tail electrons ($\frac{1}{2}mv_e^2 \simeq 80$ eV, $v_e \simeq 5\times 10^8$ cm/sec).

The plasma potential and the electric field profiles are also measured at different background pressures. As the neutral pressure is increased, the ambipolar electric field becomes stronger and spatially more localized (Fig. 18); the electric field also propagates at a much higher velocity. Figure 19 shows the time-of-flight measurements of the electric field peak for different background pressures. At $P \simeq 4\times 10^{-4}$ Torr, the average propagation velocity (measured at the peak) is 2.8×10^6 cm/sec. The newly created, cold ($kT_i \leqslant 0.5$ eV, $v_i \simeq 1\times 10^5$ cm/sec) ions cannot effectively interact with the high velocity, propagating electric field due to their inertia. The slower ions lag behind the electric field, and are not accelerated. A similar effect has been

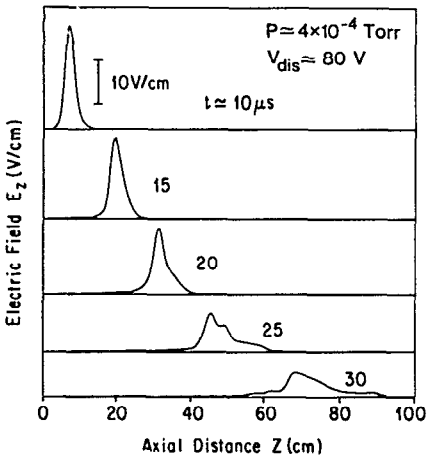

FIG. 18. Evolution of the axial electric field (E_z) profile at high background neutral pressure ($P \simeq 4 \times 10^{-4}$).

observed in a laser-pellet experiment by Tan and Borovsky[59] who have reported a reduction in the streaming energy of fast ions at high background gas pressures ($P \geqslant 10^{-3}$ Torr).

B. Final state of expanding plasma

The expanding plasma reaches the end of the chamber in $t \simeq 100\,\mu$sec, and is collected by a large conducting endplate. The copper endplate is normally grounded, but can be biased with respect to the chamber wall. When grounded, the end plate collects ions and reflects electrons. The net current through the plasma is small (< 100 mA $\simeq 1\%$ of the discharge current). Figure 20 shows the time evolution of the plasma potential profiles along the axis. As a function of time, the potential profile develops a well-defined double layer. Most of the electrostatic field remains localized within the double layer which propagates away from the source at decreasing velocity ($v \ll c_s$) and amplitude. At early times ($t < 100\,\mu$sec), the potential downstream of the double layer decreases monotonically as a function of z; but at later times ($t > 200\,\mu$sec), the downstream potential gradient becomes negligible.

The propagation velocity of the double layer is deduced

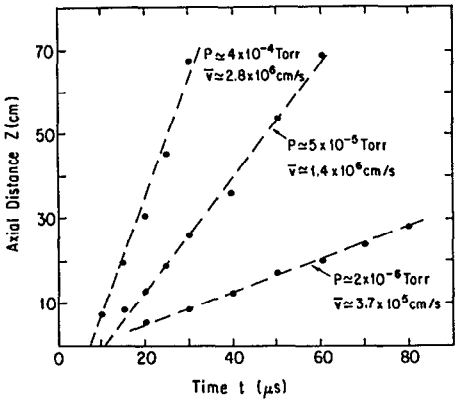

FIG. 19. The propagation of the electric field (measured at the peak) at different background neutral pressures. The slope of the dashed lines are the average propagation velocities.

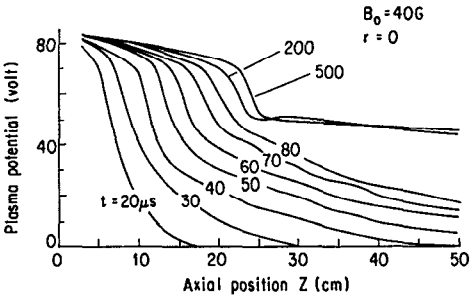

FIG. 20. Measured temporal evolution of the axial plasma potential profiles. Note the formation of a steady-state potential double layer at late times ($t > 200\,\mu$sec).

from time-of-flight measurements of both the plasma potential and the ion saturation current independently. As previously mentioned, the propagation velocity is independent of the tail electron energy, but does depend on the initial density gradient of the source plasma which is controlled by the density of the injected neutral beam. At a constant discharge current (constant tail electron density), as the neutral gas density is increased the density of Maxwellian electrons n_M (secondary electrons) and ions in the source increases. Thus, n_{tail}/n_M is reduced as the neutral beam density is increased. Figure 21 shows qualitatively the propagation of the double layer for three different ratios of n_{tail}/n_M. As n_M increases (n_{tail}/n_M decreases), the double layer propagates faster. The initial propagating velocity of the double layer can range from 1.5×10^5 to 3.7×10^5 cm/sec which corresponds roughly to the ion sound speed in the Maxwellian population ($kT_e \simeq 4$ eV, and $C_s \simeq 3 \times 10^5$ cm/sec). Hence, for a constant value of n_{tail}, the velocity of the double layer is determined solely by the pressure gradient of the Maxwellian electrons. In contrast to our experimental observations, however, the theory[44,57] for a semi-infinite, two-electron-temperature, expanding plasma predicts the double layer to propagate at C_s into the unperturbed, stationary plasma (i.e., in a direction opposite to the expansion). The apparent discrepancy could be due to the finite velocity of

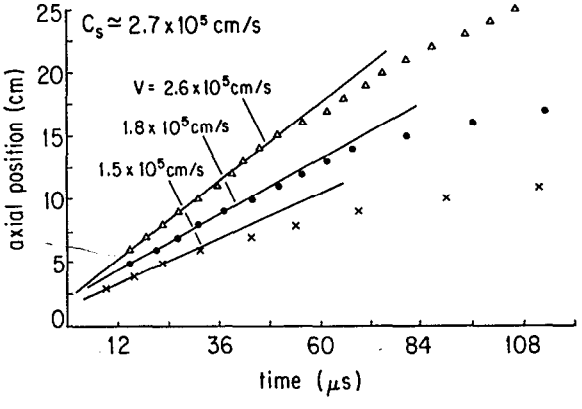

FIG. 21. Time-of-flight measurements of the propagating double layer as a function of initial source density of Maxwellian electrons (n_M). For a constant value of n_{tail} as n_M is increased, the Maxwellian electron pressure gradient increases and the double layer propagates faster.

the ions upstream of the double layer, which in our case have supersonic velocities ($v > C_s$).

1. Evolution of double layer

The initially propagating double layer slows down and eventually stagnates. At $t \geqslant 200\,\mu$sec, the double layer ($\Delta\phi \simeq 20$–60 V, $\Delta z \simeq 2.5$–5 cm $\simeq 50$–$100\,\lambda_D$) reaches a steady state. The double layer maintains its steady-state condition till the end of the discharge pulse ($\Delta t \simeq 1$ msec) which is much longer than the ion transit time ($t \simeq 150\,\mu$sec) through the device. When the discharge pulse is switched off, the double layer decays in less than 10 μsec. Some typical characteristics of the steady-state double layer are displayed in Fig. 22. The plasma potential profile is differentiated once with respect to z to obtain the axial electric field $E_z = -d\phi_p/dz$. The excess space charge density $\Delta n = n_i - n_e$ is deduced from the gradient of the electric field ($\Delta n = \epsilon_0 dE_z/e\,dz$), and then normalized to the average plasma density ($n_a \simeq 7 \times 10^9$ cm^{-3}). The maximum, normalized, excess charge density is $\Delta n/n_a \simeq 0.1\%$ which is smaller than $(m_e/m_i)^{1/2} \simeq 0.4\%$. As will be shown later, the double layer is essentially currentless (i.e., relative electron-ion drift is zero), and the net current through the plasma is very small (of the order of ion saturation current). In addition, the double layer contains no trapped or counter streaming ions. The existence of steady-state, currentless double layers has been predicted theoretically.[60,61] However, with the exception of this work,[46] currentless double layers have only been observed in the vicinity of a strong magnetic field gradient.[62,63]

Two-dimensional (z and r) plasma potential profiles are mapped over a half-plane 30×75 cm^2 containing 286 spatial data points. Figure 23 shows contours of constant plasma potential (a) and the radial plasma density profile (b) at $t = 500\,\mu$sec. The potential contours clearly display the double layer structure which forms at $z \simeq 27$ cm. In the central region of plasma (diam $\simeq 10$ cm), the electric field is parallel to the axial magnetic field. Upstream of the double layer, the electric field at the edge of the plasma column is radially

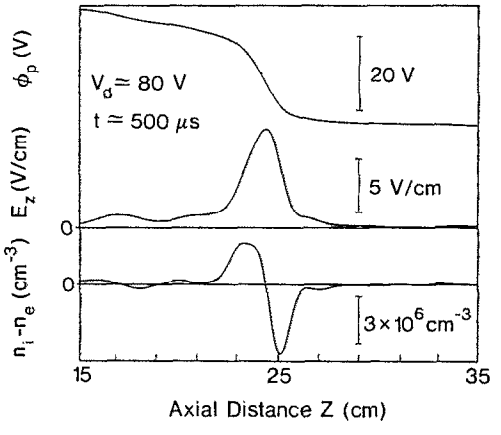

FIG. 22. Measured axial potential profile of the double layer. The axial electric field E_z and the space charge separation $\Delta n \simeq n_i - n_e$ are calculated from the potential profile.

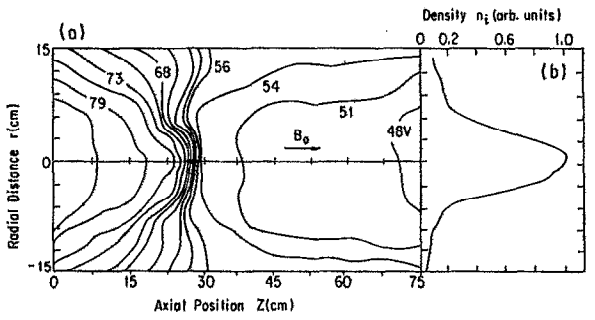

FIG. 23. (a) Contours of constant plasma potential ($\Delta\phi \simeq 3$ V between contours) showing the steady-state double layer at $t \simeq 500\,\mu$sec, and $B_0 = 45$ G. (b) The radial plasma density profile (arb. units) is measured at $z \simeq 60$ cm, $B_0 \simeq 45$ G.

outward; and downstream, it is radially inward (perpendicular to the axial B field). As the magnetic field is lowered, the radially inward electric field begins to change direction. At very low magnetic fields ($B \leqslant 3$ G), the electric field becomes radially outward everywhere. Furthermore, the axial electric field E_z decreases and its profile broadens along the z axis as the magnetic field is reduced presumably due to a decrease in plasma density (an increase in the Debye length).

As before, the absolute electron density is measured with the microwave resonator, while the relative density of tail to Maxwellian electrons is measured with the small, disc-shaped (3 mm diam) Langmuir probe. Since space-charge separation is small, ion and electron densities are identical. At the source, the measured, relative density ratio of tail to Maxwellian electrons (n_{tail}/n_M) is 1%–5%. This ratio is controlled by the density of the injected neutral gas. Figure

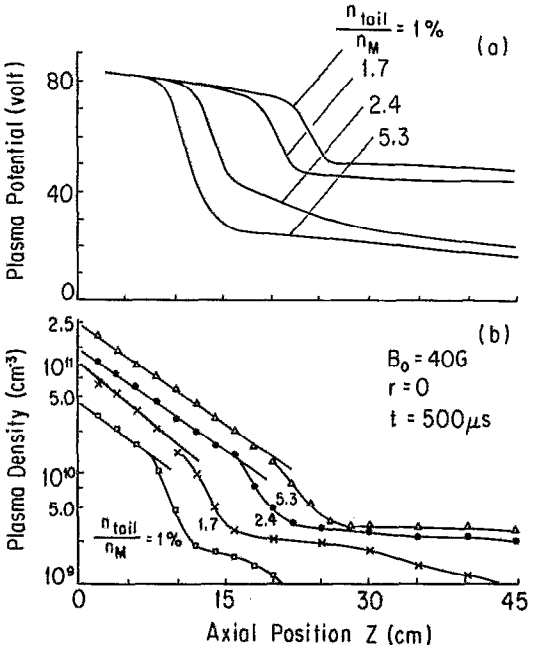

FIG. 24. (a) Steady-state plasma potential profiles along the z axis for different values of n_{tail}/n_M at the source. (b) The corresponding plasma density profiles [$\log(n)$ vs z].

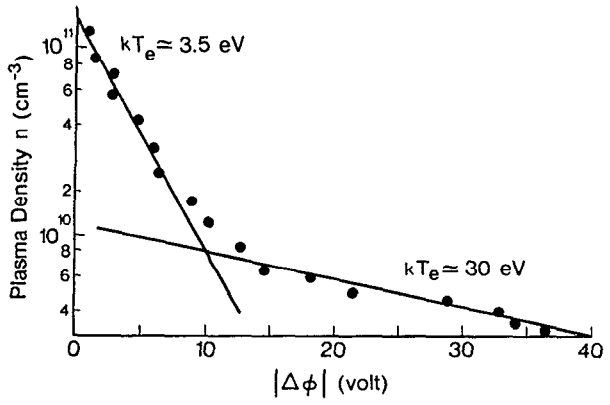

FIG. 25. Plot of plasma density (log scale) versus the change in plasma potential. The slope of the curve is a measure of the parallel electron temperature. The plot shows the presence of two distinct electron populations.

24 shows the steady-state plasma potential (a), and the corresponding density profiles (b) along the central axis for different values of $n_{\rm tail}/n_{\rm M}$. The position and the amplitude of the double layer depend on the ratio $n_{\rm tail}/n_{\rm M}$ at the source. As the density of the Maxwellian electrons is reduced with respect to that of the tail electrons, the double layer moves back toward the source and its amplitude increases.

As shown in Fig. 24(b), the plasma density decreases almost exponentially (linearly on the vertical log scale) away from the source. A steady-state, strong density gradient is created, and the electrons remain in an electrostatic equilibrium with the stationary electric field ($E_{\rm DL}$) of the double layer; i.e., $\nabla p_e = neE_{\rm DL}$. By plotting the log of the electron density versus the change in plasma potential, one can estimate the parallel temperature of the electrons from the slope of the curve [$kT_e = e\Delta\phi/\ln(n/n_0)$, the Boltzmann relation]. Figure 25 is a plot of electron density versus the change in plasma potential $|\Delta\phi|$. It shows two distinct electron temperatures. On the high potential side, the estimated parallel temperature for the electrons is about 3.5 eV which agrees well with $kT_e \simeq 4$ eV as measured with a Langmuir probe. At the double layer, the effective parallel electron temperature is about 30 eV. Since the energetic tail electrons have an isotropic distribution, the expected average parallel energy is roughly one-third of total energy (one-third of 80 eV) or 27 eV. The potential drop ($\Delta\phi \simeq 20$–60 V) at the double layer is of the order of "free" electron parallel temperature ($\simeq 30$ eV); therefore, this is a weak[64] double layer.

At the source, the Maxwellian electrons dominate ($n_{\rm tail}/n_{\rm M} \leqslant 0.05$). As the distance from the source increases, the Maxwellian electrons are retarded by the electrostatic field; $n_{\rm M}$ decreases faster than $n_{\rm tail}$, and $n_{\rm tail}/n_{\rm M}$ increases as confirmed by Langmuir probe measurements. Finally, the energetic electrons dominate the electron population. The double layer forms at a position where the transition in electron population occurs ($n_{\rm tail} \geqslant n_{\rm M}$), as predicted by earlier theoretical studies.[55,56] Obviously, the higher the density of Maxwellian electrons, the farther away from the source the transition would occur; this is why the position of the double layer is controlled by the relative densities of the two electron species. During the discharge, the neutral gas density varies in time (Fig. 2). As a function of time, the gas density increases, reaches its maximum at $t \simeq 500\,\mu$sec, and then decreases. Consequently, $n_{\rm tail}/n_{\rm M}$ decreases initially in time ($t < 500\,\mu$sec), and then increases for $t > 500\,\mu$sec. These variations in $n_{\rm tail}/n_{\rm M}$ are reflected in the late ($t > 200\,\mu$sec) evolution of the double layer. As $n_{\rm tail}/n_{\rm M}$ decreases due to an increase in $n_{\rm M}$, the steady-state double layer moves farther away from the source ($\Delta z \simeq 2$ cm, $\Delta t \simeq 300\,\mu$sec); and as $n_{\rm tail}/n_{\rm M}$ increases, the double layer returns toward the source ($\Delta z \simeq -4$ cm, $\Delta t \simeq 500\,\mu$sec).

2. Ion and electron distribution

As expected, the double layer accelerates ions to form a low-density, high energy beam in the downstream region. Upon impact with the endplate, the ions are neutralized. The parallel ion distribution function is measured with the directional energy analyzer. Near the source ($z < 5$ cm), only cold ($kT_i < 1$ eV) ions are observed. Away from the source, the ions are accelerated to supersonic velocities ($v > C_s \simeq 3.1 \times 10^5$ cm/sec) before entering the double layer. When the ions traverse the double layer, they are further accelerated by the strong, localized electric field. On the low potential side, the ions have a beamlike distribution function with a small energy spread ($kT_b \simeq 0.1$ eV). The kinetic energy of the ion beam is equal to the potential drop across the double layer ($\frac{1}{2}Mv_i^2 \simeq e\Delta\phi$). This is in contrast to our earlier observations during the transient plasma expansion process where the streaming energy of ions exceeded the electrostatic potential drop ($\frac{1}{2}Mv^2 > e\Delta\phi$). There are no trapped or stationary background ions on the low potential side. The angular beam divergence ($\Delta\theta \simeq 12°$) is also wider than those measured in the earlier times (e.g., $\Delta\theta \simeq 7°$ at $t \simeq 50\,\mu$sec). The broadening is partly due to a lower parallel beam velocity, and partly due to the radially outward electric fields which develop near the source at late times (see Fig. 23).

The low-potential region consists of a steady-state, monoenergetic ion beam neutralized by the retarded tail electrons which were able to overcome the double layer potential ($\frac{1}{2}mv_\parallel^2 \geqslant e\Delta\phi$). There are no stationary background ions present. The retarded electrons are reflected by the grounded endplate and are accelerated back toward the source by the double layer. The electron distribution function on the low potential side is measured along the z axis. The microchannel plate of the directional analyzer is biased to the local plasma potential, and a rapidly swept voltage ramp $V(t)$ ($dV/dt \simeq 10$ V/μsec) is applied to the discriminator grid. The positively biased collector current is averaged over 10 shots and stored. The collector I-V curve is differentiated and smoothed to obtain $v^2 f(v)$ which when divided by v^2 yields the electron distribution function in one dimension.[65] The directional analyzer is rotated by 180° in increments of $\Delta\theta \simeq 10°$ to obtain the complete two-dimensional distribution function $f(v,\theta)$ of the electrons streaming away from the source. The data in polar coordinates is converted to Cartesian coordinates $f(v_z,v_x)$ for display purposes. Since the system is symmetric with respect to the z axis, it is assumed that $f(v_z,v_x) = f(v_z,v_y) = f(v_z,v_\perp)$. The normalized

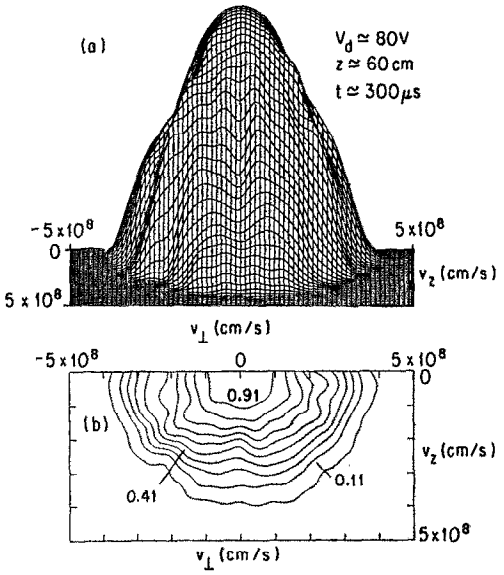

FIG. 26. Electron distribution function downstream of the double layer. (a) The normalized, three-dimensional view of $f(v_z, v_\perp)$ on a linear scale. The external magnetic field $B_0 \simeq 30$ G is in the z direction. (b) Contours of constant $f(v_z, v_\perp)$, 10% change per contour.

electron distribution function at $t \simeq 300\ \mu$sec is shown in Fig. 26. The measurements are performed at $z \simeq 60$ cm, downstream of the double layer ($\Delta\phi \simeq 25$ V, $z \simeq 27$ cm). The electron distribution function is isotropic with a broad velocity spread. The effective electron temperature (half-width at $1/e$ of maximum) on the low potential side is $kT_e \simeq 20$ eV which is less than the measured parallel electron temperature at the double layer ($kT_e \simeq 30$ eV).

3. Plasma current

The plasma current is measured externally as a function of the endplate bias. Normally, the endplate and the cathode are grounded, and the measurements show that a very small net current (of the order of ion saturation current) flows between the source and the endplate. Most of the discharge current (98%) flows between the cathode and the anode within the source. When the net current through the plasma is reduced to zero by floating the anode–cathode structure, no significant changes (to within 10%) are observed in the position, amplitude, or width of the double layer even though the absolute value of the plasma potential with respect to the chamber wall changes. In contrast, when the endplate is biased positively with respect to the cathode to draw electron current, the double-layer amplitude decreases and finally disappears as the bias voltage is increased (Fig. 27). The positively biased endplate collects the retarded electrons, reduces the excess negative space charge on the low-potential side, and weakens the double layer. A negative bias on the endplate has very little effect on the double layer because (a) the negatively biased endplate does not affect electrons, and (b) the excess collected ion current is insignificant.

As previously mentioned, the double-layer amplitude depends on the ratio n_{tail}/n_M. When n_{tail}/n_M decreases be-

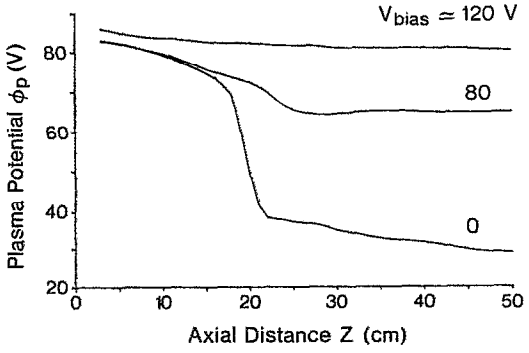

FIG. 27. Measured axial potential profiles at $t \simeq 500\ \mu$sec for three different values of the endplate bias. As the bias is increased, the endplate collects more electrons which reduces the excess negative space charge and weakens the double layer.

cause of an increase in densities of secondary electrons and ions, the ion flux into the low-potential region increases. The additional ions apparently neutralize some of the negative space charge and thereby reduce the amplitude of the potential drop. Conversely, when n_{tail}/n_M increases, the source ion density and its flux into the low-potential side is reduced, and the double layer becomes stronger. At high background pressures ($P > 2\times10^{-5}$ Torr), where significant ionization does occur everywhere within the plasma column, no steady-state double layer is observed. Since ions are created uniformly in the plasma column, they readily neutralize any excess negative charge buildup which is essential in establishing the double layer.

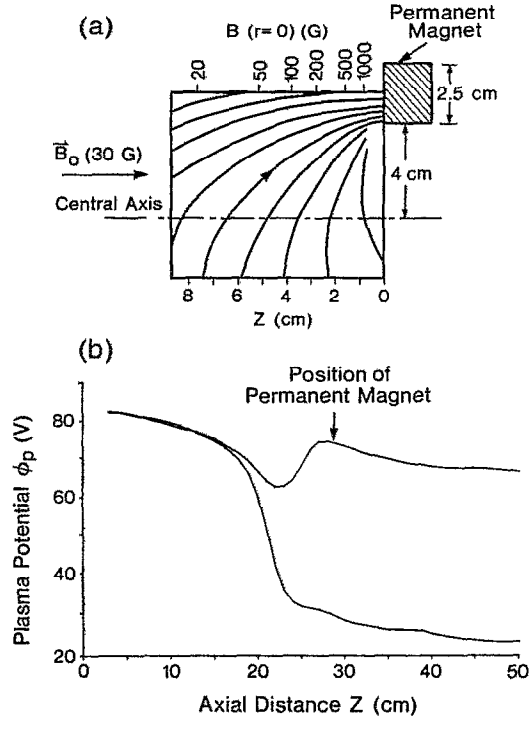

FIG. 28. (a) Magnetic field line profiles and axial field strength of the permanent magnet. (b) The potential profiles with and without the magnet. The permanent magnet reflects the electrons and destroys the double layer.

The role of the energetic electrons in establishing the double layer is further demonstrated by a simple experiment. A strong SmCo permanent magnet (2.5 cm diam and 2 cm length, $B_{max} \simeq 3000$ G) is suspended downstream of the double layer. The magnet whose dipole moment is parallel to the chamber axis is located at a distance of 28 cm from the source. To minimize plasma perturbation, the magnet is placed at the edge of the plasma column, radially offset by 4 cm from the central axis of the plasma. The magnetic field lines of the permanent magnet and the field strength variations along the axis of the magnet are measured and displayed in Fig. 28(a). The magnetic dipole and the uniform, parallel axial field form a magnetic mirror. Figure 28(b) shows the double-layer potential profile with and without the permanent magnet. In the presence of the magnet, the double layer is observed to be annihilated because of magnetic reflection of the energetic electrons in the low-potential side. The low energy electrons are mainly reflected by the residual potential drop rather than by magnetic mirroring since $B_{magnet} \leqslant B_0$ at $z \leqslant 20$ cm.

IV. CONCLUSIONS AND SUMMARY

When a Maxwellian plasma containing a small number of energetic tail electrons expands into vacuum, the energetic electrons accelerate a small fraction of ions to energies above that of the energetic electrons. The plasma expansion is driven by the electron pressure gradient. During the expansion, the two electron species separate with the tail electrons dominating the expansion front. Initially, a large electric field ($\Delta\phi/\Delta z \simeq 20$ V/cm) develops at the plasma–vacuum interface due to space-charge separation. The propagating, ambipolar electric field whose amplitude is controlled by the energy of the tail electrons accelerates ions along the axial magnetic field. The energetic ions have a beamlike distribution with a high streaming energy and a small angular divergence. The maximum, measured ion beam energy scales linearly with the tail electron energy. There exists a small number of ions whose streaming energy exceeds the electrostatic potential drop of the electric field ($\frac{1}{2}Mv^2 > e\Delta\phi$). The excess ion energy is due to ion transit time effect. When the propagating velocity of the electric field becomes comparable to the ion velocity, the ion transit time through the field increases. As a result, the ions spend a longer time under the influence of the field, and are accelerated to higher energies.

The space charge potential set up by the energetic tail electrons traps the much colder Maxwellian electrons which form a slow moving front behind the expansion front. The slow expansion front is marked by a double layer which propagates away from the source at a velocity comparable to the ion sound speed in the cold plasma component. The region downstream of the double layer is predominantly populated by the tail electrons, and the cold, Maxwellian electron population is virtually negligible since the downstream region is 25–50 V more negative than the upstream region. At the double layer, strict charge neutrality is violated. The maximum excess charge density normalized to the local plasma density is $\Delta n/n \simeq -0.1\%$.

At late times ($t > 200\,\mu$sec), the propagating double layer slows down and eventually stagnates. A steady-state, current-free double layer is formed whose final position and amplitude are determined by the initial relative densities of the two electron populations in the source. The steady-state double layer persists till the end of the discharge pulse ($\Delta t \simeq 1$ msec $\gg$ ion transit time $\simeq 150\,\mu$sec). The double layer is weak[64] ($e\Delta\phi/kT_e \leqslant 10$) and contains no trapped or counter-streaming ion populations. The formation of the double layer is due to the self-consistent separation of the two electron species. On the low potential side, the double layer produces a monoenergetic ion beam with no stationary background plasma. The double layer is annihilated when a field-aligned electron current is drawn through the plasma.

As a function of increasing background gas pressure, the ambipolar electric field becomes stronger, more localized, and its propagating velocity increases. At high pressures ($P \geqslant 4\times10^{-4}$ Torr), no energetic ions are detected at the expansion front even though both the ambipolar electric field and the plasma front propagate away from the source at speeds approaching 10^7 cm/sec. The energetic electrons ionize the background gas, and create an ionization front. It is this front which propagates at extremely high velocities ($v \simeq 10^7$ cm/sec). The newly created ions rapidly neutralize the tail electrons at the ionization front and allow the rapid propagation of electrons through the neutral gas. The slower, heavier ions cannot effectively interact with the ambipolar electric field at the ionization front, and are not accelerated. No steady-state double layer is observed at higher background pressures ($P > 2\times10^{-5}$ Torr).

The possibilities of future work include detailed study of the observed low frequency fluctuations on the low potential side to fully understand the origin and the effects of the fluctuations on the modulation of ion streaming energy. In addition, various tail electron velocity distributions (e.g., a beam or a hot Maxwellian) can be used to study the effects of different electron distribution functions on ion acceleration process. Another exciting possibility is the study of interaction of the energetic electrons with the background gas, and the role of the background neutral gas on charge neutralization and ion acceleration. With some modifications of the present experimental setup, the expansion of two counter-streaming plasmas into each other, and the interaction of a supersonically streaming plasma with a neutral gas cloud or with various magnetic configurations (e.g., converging, diverging, or transverse field) could also be investigated.

ACKNOWLEDGMENTS

The authors wish to thank Drs. A. Kuthi, P. Cheung, J. M. Urrutia, D. Needelman, L.-Y. Chan, and P. Straus for useful discussions. Expert technical assistance by Mr. A. Boyarsky and Mr. M. Wilson is also acknowledged.

This work was supported by National Science Foundation Grants No. ATM87-02793 and No. PHY87-13829, and National Aeronautics and Space Administration Grant No. NAGW 1570.

[1]A. V. Gurevich, L. V. Pariiskaya, and L. P. Pitaevskii, Sov. Phys. JETP **22**, 449 (1966).
[2]V. G. Eselevich and V. G. Fainshtein, Sov. Phys. JETP **52**, 441 (1980).

[3]A. W. Ehler, J. Appl. Phys. **46**, 2464 (1975).
[4]U. Samir, K. H. Wright, Jr., and N. H. Stone, Rev. Geophys. Space Phys. **21**, 1631 (1983).
[5]R. Tanberg, Phys. Rev. **35**, 1080 (1930).
[6]E. Kobel, Phys. Rev. **36**, 1636 (1930).
[7]A. A. Plyutto, Sov. Phys. JETP **12**, 1106 (1961).
[8]P. M. Campbell, R. R. Johnson, F. J. Mayer, L. V. Powers, and D. C. Slater, Phys. Rev. Lett. **39**, 274 (1977).
[9]R. L. Morse and C. W. Nielson, Phys. Fluids **16**, 909 (1973).
[10]N. H. Stone, K. H. Wright, Jr., U. Samir, and K. S. Hwang, Geophys. Res. Lett. **15**, 1169 (1988).
[11]A. V. Gurevich, L. P. Pitaevskii, and V. V. Smirnova, Space Sci. Rev. **9**, 805 (1969).
[12]U. Samir, N. H. Stone, and K. H. Wright, Jr., J. Geophys. Res. **91**, 277 (1986).
[13]K. H. Wright, Jr., N. H. Stone, and U. Samir, J. Plasma Phys. **33**, 71 (1985).
[14]J. S. Pearlman, J. J. Thomson, and C. E. Max, Phys. Rev. Lett. **38**, 1397 (1977).
[15]P. Wagli and T. P. Donaldson, Phys. Rev. Lett. **40**, 875 (1978).
[16]J. Nuckolls, L. Wood, A. Theiessen, and G. Zimmerman, Nature **239**, 139 (1972).
[17]K. A. Brueckner, P. M. Campbell, and R. A. Grandey, Nucl. Fusion **15**, 471 (1975).
[18]F. Begay and D. W. Forslund, Phys. Fluids **25**, 1675 (1982).
[19]N. Singh and R. W. Schunk, J. Geophys. Res. **87**, 9154 (1982).
[20]P. M. Banks and T. E. Holzer, J. Geophys. Res. **74**, 6317 (1969).
[21]J. E. Crow, P. L. Auer, and J. E. Allen, J. Plasma Phys. **14**, 65 (1975).
[22]T. Whelan and C. K. Goertz, Geophys. Res. Lett. **14**, 68 (1987).
[23]R. W. Schunk and E. P. Szuszczewicz, J. Geophys. Res. **93**, 12901 (1988).
[24]N. Singh and R. W. Schunk, J. Geophys. Res. **88**, 7867 (1983).
[25]J. E. Borovsky, M. B. Pongratz, R. A. Roussel-Dupre, and T.-H. Tan, Astrophys. J. **280**, 802 (1984).
[26]S. G. Alikhanov, V. G. Belan, G. N. Kichigin, and P. Z. Chebotaev, Sov. Phys. JETP **32**, 1061 (1971).
[27]S. Raychaudhuri, J. Hill, H. Y. Chang, E. K. Tsikis, and K. E. Lonngren, Phys. Fluids **29**, 289 (1986).
[28]D. Diebold, N. Hershkowitz, T. Intrator, and A. Bailey, Phys. Fluids **30**, 579 (1987).
[29]H. Kozima, H. Shimizu, K. Yamada, T. Mieno, and K. Yamagiwa, J. Phys. Soc. Jpn. **57**, 1136 (1988).
[30]N. Wild, R. L. Stenzel, and W. Gekelman, Geophys. Res. Lett. **10**, 682 (1983).
[31]R. L. Merlino and N. D'Angelo, J. Plasma Phys. **37**, 185 (1987).
[32]R. L. Stenzel, R. Williams, R. Aguero, K. Kitazaki, A. Ling, T. McDonald, and J. Spitzer, Rev. Sci. Instrum. **53**, 1027 (1982).
[33]P. Korn, T. C. Marshall, and S. P. Schlesinger, Phys. Fluids **13**, 517 (1970).
[34]C. Chan, N. Hershkowitz, A. Ferreira, T. Intrator, B. Nelson, and K. Lonngren, Phys. Fluids **27**, 226 (1984).
[35]V. G. Eselevich and V. G. Fainshtein, Sov. Phys. JETP **7**, 271 (1981).
[36]D. M. Villeneuve, G. D. Enright, M. D. J. Burgess, R. Fedosejevs, and M. C. Richardson, Phys. Rev. Lett. **47**, 515 (1981).
[37]C. Joshi, M. C. Richardson, and G. D. Enright, Appl. Phys. Lett. **34**, 625 (1979).
[38]R. Decoste and B. H. Ripin, Phys. Rev. Lett. **40**, 34 (1978).
[39]W. C. Mead, R. A. Haas, W. L. Kruer, D. W. Kornblum, J. D. Lindl, D. R. MacQuigg, and V. C. Rupert, Phys. Rev. Lett. **37**, 489 (1976).
[40]J. D. Hares, J. D. Kilkenny, M. H. Key, and J. G. Lunney, Phys. Rev. Lett. **42**, 1216 (1979).
[41]L. M. Wickens, J. E. Allen, and P. T. Rumsby, Phys. Rev. Lett. **41**, 243 (1978).
[42]A. Gurevich, D. Anderson, and H. Wilhelmsson, Phys. Rev. Lett. **42**, 769 (1979).
[43]R. B. Torbert, Adv. Space Res. **8**, 39 (1988).
[44]N. Singh, IEEE Trans. Plasma Sci. **PS-17**, 116 (1989).
[45]G. Hairapetian and R. L. Stenzel, Phys. Rev. Lett. **61**, 1607 (1988).
[46]G. Hairapetian and R. L. Stenzel, Phys. Rev. Lett. **65**, 175 (1990).
[47]J. B. Cross and J. J. Valentini, Rev. Sci. Instrum. **53**, 38 (1982).
[48]J. B. Anderson, in *Molecular Beams and Low Density Gasdynamics*, edited by P. P. Wegener (Dekker, New York, 1974), p. 9.
[49]J. Marshall, in *Proceedings of Fourth Lockheed Symposium on Magnetohydrodynamics, Plasma Acceleration*, edited by S. W. Kash (Stanford U. P., Stanford, California, 1970), p. 60.
[50]S. C. Brown, *Basic Data of Plasma Physics* (MIT Press, Cambridge, MA, 1966).
[51]L. Spitzer, Jr., *Physics of Fully Ionized Gases* (Interscience, New York, 1962), p. 113.
[52]J. M. Urrutia and R. L. Stenzel, Phys. Rev. Lett. **57**, 715 (1986).
[53]R. L. Stenzel, Rev. Sci. Instrum. **47**, 603 (1976).
[54]A. V. Gurevich and A. P. Meshcherkin, Sov. Phys. JETP **53**, 937 (1981).
[55]B. Bezzerides, D. W. Forslund, and E. L. Lindman, Phys. Fluids **21**, 2179 (1978).
[56]M. A. True, J. R. Albritton, and E. A. Williams, Phys. Fluids **24**, 1885 (1981).
[57]J. Denavit, Phys. Fluids **22**, 1384 (1979).
[58]Y. Kishimoto, K. Mima, T. Watanabe, and K. Nishikawa, Phys. Fluids **26**, 2308 (1983).
[59]T.-H. Tan and J. E. Borovsky, J. Plasma Phys. **35**, 239 (1986).
[60]D. P. Stern, J. Geophys. Res. **86**, 5839 (1981).
[61]F. W. Perkins and Y. C. Sun, Phys. Rev. Lett. **46**, 115 (1981).
[62]Y. Nakamura and R. L. Stenzel, in *Proceedings of the Symposium on Plasma Layers*, edited by P. Michelsen and J. Juul Rasmussen (Risø National Laboratory, Roskilde, Denmark, 1982), p. 153.
[63]R. Hatakeyama, Y. Suzuki, and N. Sato, Phys. Rev. Lett. **50**, 1203 (1983).
[64]L. P. Block, Astrophys. Space Sci. **55**, 59 (1978).
[65]R. L. Stenzel, W. Gekelman, N. Wild, J. M. Urrutia, and D. Whelan, Rev. Sci. Instrum. **54**, 1302 (1983).